High-temperature high-pressure calorimeter for studying gram-scale heterogeneous chemical reactions

B. P. MacLeod, P. A. Schauer, K. Hu, B. Lam, D. K. Fork, and C. P. Berlinguette

Citation: Review of Scientific Instruments **88**, 084101 (2017); doi: 10.1063/1.4999361
View online: http://dx.doi.org/10.1063/1.4999361
View Table of Contents: http://aip.scitation.org/toc/rsi/88/8
Published by the American Institute of Physics

Articles you may be interested in

Linear servomotor probe drive system with real-time self-adaptive position control for the Alcator C-Mod tokamak
Review of Scientific Instruments **88**, 073501 (2017); 10.1063/1.4990043

Measurement of contact angles of microscopic droplets by focal length method
Review of Scientific Instruments **88**, 083701 (2017); 10.1063/1.4996781

Measurement of the velocity of neutral fragments by the "correlated ion and neutral time of flight" method combined with "velocity-map imaging"
Review of Scientific Instruments **88**, 083101 (2017); 10.1063/1.4991828

A high voltage pulse generator based on silicon-controlled rectifier for field-reversed configuration experiment
Review of Scientific Instruments **88**, 083507 (2017); 10.1063/1.4997077

The world's smallest capacitive dilatometer, for high-resolution thermal expansion and magnetostriction in high magnetic fields
Review of Scientific Instruments **88**, 083903 (2017); 10.1063/1.4997073

A surface science compatible epifluorescence microscope for inspection of samples under ultra high vacuum and cryogenic conditions
Review of Scientific Instruments **88**, 083702 (2017); 10.1063/1.4997953

Obstruction free access
optical table with integrated cryocooler

Various Objective Options
attocube
pioneers of precision
attoDRY800
• Cryogenic Temperatures
• Ultra-Low Vibration
• Optical Table Included
• Fast Cooldown
5% DISCOUNT
on all nanopositioners purchased for your attoDRY800 set-up*
Coupon Code: PTJAD800
*valid for quotations issued before November, 2017

High-temperature high-pressure calorimeter for studying gram-scale heterogeneous chemical reactions

B. P. MacLeod,[1,2] P. A. Schauer,[1] K. Hu,[1] B. Lam,[1] D. K. Fork,[3] and C. P. Berlinguette[1,2,4,a)]
[1]*Department of Chemistry, University of British Columbia, Vancouver, British Columbia V6T 1Z1, Canada*
[2]*Stewart Blusson Quantum Matter Institute, University of British Columbia, Vancouver, British Columbia V6T 1Z4, Canada*
[3]*Google Inc., 1600 Amphitheatre Parkway, Mountain View, California 94043, USA*
[4]*Department of Chemical and Biological Engineering, University of British Columbia, Vancouver, British Columbia V6T 1Z3, Canada*

(Received 22 April 2017; accepted 7 August 2017; published online 22 August 2017)

We present an instrument for measuring pressure changes and heat flows of physical and chemical processes occurring in gram-scale solid samples under high pressures of reactive gases. Operation is demonstrated at 1232 °C under 33 bars of pure hydrogen. Calorimetric heat flow is inferred using a grey-box non-linear lumped-element heat transfer model of the instrument. Using an electrical calibration heater to deliver 900 J/1 W pulses at the sample position, we demonstrate a dynamic calorimetric power resolution of 50 mW when an 80-s moving average is applied to the signal. Integration of the power signal showed that the 900 J pulse energy could be measured with an average accuracy of 6.35% or better over the temperature range 150-1100 °C. This instrument is appropriate for the study of high-temperature metal hydride materials for thermochemical energy storage. *Published by AIP Publishing.* [http://dx.doi.org/10.1063/1.4999361]

I. INTRODUCTION

The study of thermochemical energy storage (TES) materials operating above 500 °C is motivated by the increased Carnot efficiency that can be achieved by operating concentrating solar power plants at elevated temperatures.[1] Metal hydrides exhibit reversible, endothermic dehydrogenation reactions appropriate for TES,[2,3] and numerous metal hydrides decompose in the 500-1150 °C temperature range.[3] Several metal hydrides require high pressures of hydrogen to drive the exothermic rehydrogenation necessary to recover the stored thermal energy, as shown by the dissociation pressure curves in Fig. 1.

By resolving solid-solid and solid-liquid phase changes in addition to kinetic and thermodynamic data for heterogeneous reactions, variable-pressure calorimetric measurements can provide richer data for the study of candidate TES reactions than the more commonly employed thermogravimetric measurements. For example, a study employing simultaneous calorimetry and thermogravimetry found an irreversible solid-state transition between polymorphs of $Mg(BH_4)_2$ at 200 °C that could be detected via calorimetry but produced no thermogravimetric analysis (TGA) signal.[5] In that study, calorimetry also provided information about decomposition reaction steps that were not clearly evident from the gravimetric data alone.

Constructing calorimeters that operate at high temperatures and high hydrogen pressures poses numerous engineering challenges. Few materials are available that retain strength, pressure integrity, and chemical inertness under these extreme conditions. Heater elements and temperature sensors are subject to chemical attack at high temperatures, particularly by reactive gases such as hydrogen. Specialized calorimetric instruments operating either under high hydrogen pressures (>50 bars) at moderate temperatures (up to 700 °C) *or* at high temperatures (up to 1800 °C) under moderate hydrogen pressures (<10 bars) are commercially available; however, commercial instruments that operate at both high hydrogen pressures and high temperatures simultaneously are not widely available (Fig. 1; Table SI of the supplementary material). All pressures quoted here are gauge pressures. The only calorimeter apparently available for studying metal hydride materials at high pressures and temperatures is a bespoke instrument that operates at hydrogen pressures up to 200 bars and temperatures up to 600 °C.[6] Here, we present an alternative calorimeter design that enables the study of gram-scale heterogeneous chemical reactions at temperatures up to at least 1232 °C while under pure hydrogen pressures up to 33 bars. The architecture of this calorimeter enables simultaneous calorimetric and pressure measurements. This instrument can provide thermodynamic, kinetic, and material stability data from a single experiment, thereby facilitating the rapid experimental screening of metal hydride materials for thermochemical energy storage applications over an otherwise inaccessible range of operating temperatures and pressures.

II. DESIGN OBJECTIVES

To enable studies on the widest possible range of TES materials, we built an instrument that operates over broad temperature and pressure ranges, can accommodate several milliliters of the sample material, and can measure pressure changes due to gas evolution/sorption with adequate resolution to track the extent of a reaction. The chosen design objectives are outlined in Table I and our rationale is detailed further in Appendix B of the supplementary material.

a)Author to whom correspondence should be addressed: cberling@chem.ubc.ca

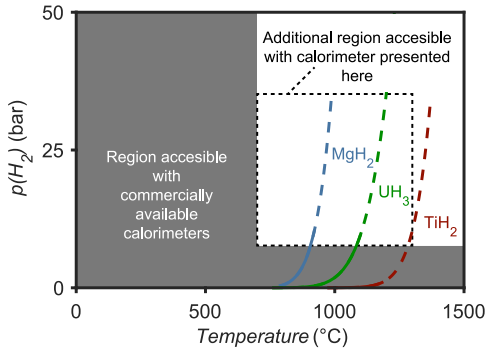

FIG. 1. Range of operation for commercially available calorimeters (grey shaded region; see Table SI of the supplementary material for details) and for the instrument reported here that enables calorimetric studies in a previously inaccessible temperature and hydrogen pressure regime. Decomposition pressure-temperature curves for selected metal hydride systems are indicated; the solid parts of the curves are data extracted from Sandrock's review of hydrogen storage materials,[4] and the dashed parts of the curves are extrapolations from that data according to the van't Hoff equation.

TABLE I. Quantitative design objectives for the calorimeter chosen to enable a wide range of studies on metal hydride TES materials.

Quantity	Design objective
Maximum operating temperature	1300 °C
Maximum operating pressure	50 bars
Sample mass	>1 g
Sample volume	10 ml
Calorimetric resolution	<100 mW
Calorimetric accuracy	<10%
Pressure measurement resolution	0.02 bars

III. CALORIMETER DESIGN

Our concept for avoiding degradation of the calorimeter heater and temperature sensors is to confine the sample solids and gases within a chemically inert, pressurized reaction tube, while placing the heater and sensors outside the tube. A tubular geometry is practical for such a pressure vessel because high purity alumina ceramic tubes that retain high strength and chemical inertness at high temperatures are readily available. As a basis for our design, we selected an alumina tube (CoorsTek AD-998) with a 0.5 in. outer diameter (OD) and 0.375 in. inner diameter (ID). We predicted that this tube will rupture at 221 bars internal pressure when the tube is at 1300 °C (see Appendix C of the supplementary material), but we did not test the system at hydrogen pressures greater than 33 bars.

Our calorimeter design is illustrated in Fig. 2. The sample and reaction tube are heated by a heater consisting of a 6 in. long, 0.55 in. ID helix of resistive wire (Sandvik Kanthal A-1). At either end of the helix, this heater terminates in a straight section of the wire which extends axially out of the isothermal jacket and connects to a power cable. To reduce the required heater input power, the heater is surrounded by a 1.5 in. ID × 9 in. OD × 12.5 in. long insulating cylinder consisting of a stack of ten insulating firebricks (Morgan Thermal Ceramics K26) cut into semi-annuli with an abrasive waterjet. This cylinder is held together by a modular liquid-cooled isothermal copper jacket. The 1.5 in. diameter cavity within the cylinder allows the heater to radiate freely in all directions, minimizing the possibility of heater failure due to localized overheating.

As shown in Fig. 2(c), an array of thermocouples samples both the radial and axial temperature gradients around the furnace hot zone. The two thermocouples closest to the heater (TC1-2) are 24 AWG R and S-type precious-metal thermocouples rated to 1480 °C (Reotemp Inc.). More economical 24 AWG N-type thermocouples rated to 980 °C (Reotemp Inc.) are anchored into the firebrick at six locations about the hot zone (TC3-8) using ceramic putty (Cotronics 7020). Six additional 24 AWG N-type thermocouples are mounted on the isothermal copper jacket, one on each face of the cylinder and four evenly spaced around the circumference, approximately halfway along the length of the cylinder.

Figure 3 provides a fluidic diagram of the instrument. To contain the sample gases, the reaction tube is sealed at

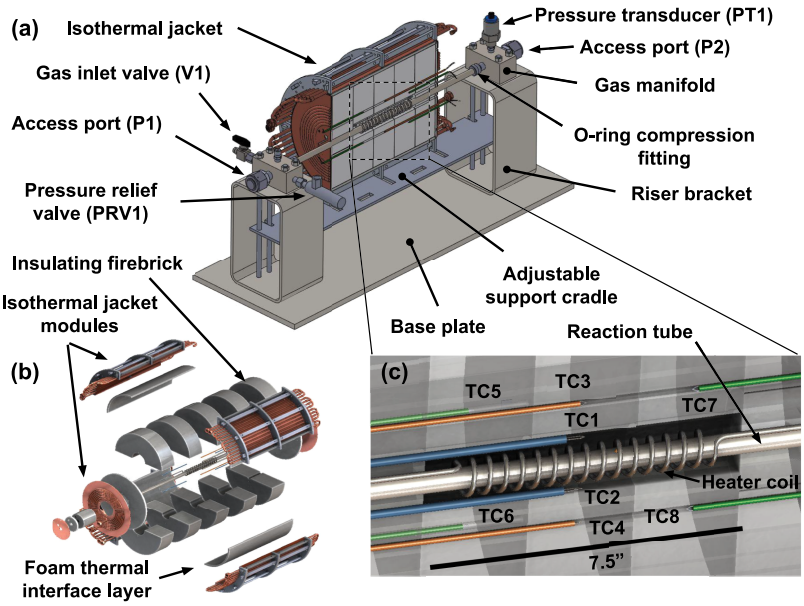

FIG. 2. Mechanical design of the calorimeter. (a) Overview of the instrument with one half of the isothermal jacket and furnace insulation cut away. (b) Exploded view of the furnace, showing the ten insulating fire bricks and the surrounding modular isothermal jacket consisting of four quadrants, two end plates, and corresponding elastic foam thermal interface layers. (c) Detailed view of the hot zone showing the locations of the heater and the eight internal thermocouples (orange, green, and blue cylinders, TC1–TC8). Not shown are six additional thermocouples epoxied to the isothermal jacket (TC9–TC14), one on each quadrant and each end plate.

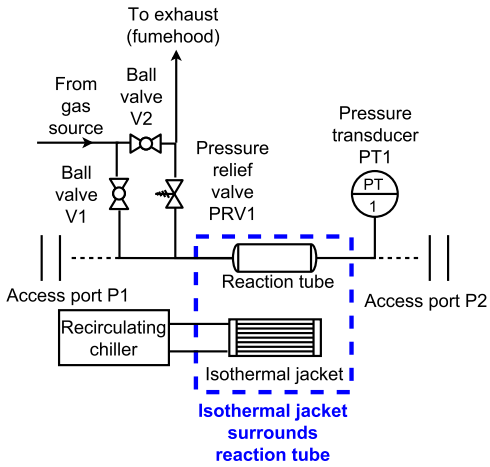

FIG. 3. Instrument fluidic diagram. Capped VCR flanges on either end of the reaction tube (P1, P2) provide access for sample and reaction tube exchange. Gases may be introduced into the reaction tube from a gas source via valve V1. PRV1 protects the system against overpressure events, while V1 and V2 can be used to manually vent the system. V1 enables the reaction tube to be isolated from the gas distribution network during experiments. PT1 provides continuous measurements of the pressure in the reaction tube. The temperature of the isothermal jacket is regulated by a recirculating chiller.

each end to a hydrogen-tolerant 316 stainless steel manifold. To facilitate reaction tube exchange, this seal is made by demountable compression fittings (Swagelok Ultra-Torr^{TM}) with hydrogen-compatible 70D Viton^{TM} O-rings. On each manifold, a copper-gasketed, 0.75 in. VCR fitting (Swagelok) provides an access port enabling easy, axial exchange of both sample crucibles and reaction tubes. One manifold provides connections for charging gases into and venting gases from the reaction tube via two ball valves (Swagelok SS-42GVCR4) and an adjustable pressure relief valve (Swagelok SS-4R3A1). A pressure transducer (Endress+Hauser Cerabar PMC131) is mounted on the other manifold. This pressure transducer was selected because it has a ceramic diaphragm compatible with reactive gases including hydrogen.

The modular isothermal jacket consists of four quadrants and two end plates fabricated from copper sheets and tubes. This jacket compresses the insulating brick cylinder via a silicone foam elastic thermal interface layer (Rogers BF2000). The temperature of the jacket is regulated to approximately ±3 °C by running coolant through the six jacket modules in parallel. A recirculating chiller (Koolance EXC-800) provides coolant at a temperature regulated by an onboard on-off controller and a thermocouple positioned on the jacket surface. This configuration provides an approximately isothermal boundary condition in order to simplify heat flow modeling. An adjustable aluminum cradle supports the entire furnace assembly and facilitates alignment of the furnace to the reaction tube.

The instrument operates using custom software built using National Instruments LabVIEW, which interfaces with several National Instruments data acquisition modules and the furnace power supply. A full electrical block diagram is provided in Fig. S2 of the supplementary material. The furnace power supply is a 720 W DC programmable supply (Keithley 2260B-30-72) that provides power to the ~0.3 Ω heater coil. A DC supply was selected because sufficiently precise AC power supplies were found to be too costly for this application. Thermocouple and transducer outputs are sampled at 1 Hz.

Samples are loaded into the calorimeter inside 0.25 in. OD × 0.188 in. ID × 4 in. long tubular alumina crucibles (Fig. S1 of the supplementary material) that provide sufficient volume to contain gram-scale quantities of the sample material. Once sample powders have been introduced into the crucible, the circular ends of the cylindrical alumina crucible are sealed with refractory putty to contain the sample. A series of holes in the crucible wall enable gas exchange between the sample and reaction tube gas space. Alumina rods of a calibrated, pre-measured length are utilized to accurately center crucibles within the hot zone of the instrument.

IV. DEMONSTRATION OF OPERATION AT HIGH TEMPERATURE AND PRESSURE

The mechanical integrity of the instrument at high temperature and pressure was demonstrated by charging the reaction tube with 27 bars of hydrogen while the entire apparatus was at ambient temperature and then stepping the heater power in 3 stages from 0 W to 350 W. The highest measured temperature (at TC1) was 1232 °C. Due to thermal expansion of the gas, the pressure reached a maximum of 33 bars. The temperature and pressure data recorded during the experiment are shown in Fig. 4. Because only a portion of the gas in the reaction tube is at elevated temperature, the pressure rise due to thermal expansion of the gas is much less than if the entire volume of gas were elevated to the sample temperature. The ratio of maximum pressure to initial pressure suggests that the average

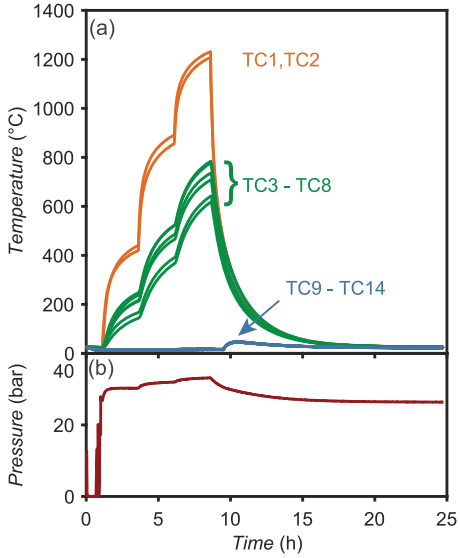

FIG. 4. Raw temperature (a) and pressure (b) data demonstrating operation at 33 bars and 1232 °C. The fourteen thermocouple temperatures are indicated in three groups (orange, green, and blue traces) because our model-based data analysis procedure makes use of only three averages of the measured temperatures, T_a, T_b, and T_s. T_a is the average of thermocouples TC1 and TC2, T_b is the average of thermocouples TC3-TC8, and T_s is the average of the six thermocouples on the isothermal jacket (see Sec. V). The chiller was turned off shortly after the main heater power steps down to 0 W, hence the rise in the cooling jacket temperatures (TC9-TC15) shortly before time = 10 h. The isothermal jacket temperature stability is approximately ±3 °C while the chiller and furnace are running.

temperature of the gas increased by a factor of 33 bars/27 bars = 1.22 or from 25 °C to around 90 °C. Based on the internal volume of 95 ml as estimated from the computer-aided design model, and a temperature-corrected pressure decrease of 0.575 bars over the course of the experiment, we estimate an average hydrogen leak-rate of 2.28 ml bars h^{-1} over the course of the experiment. The noise on the raw pressure data is of amplitude 0.005 bars.

V. INFERRING THE SAMPLE HEAT FLOW WITH A NONLINEAR LUMPED-PARAMETER MODEL

The calorimetric measurements reported here rely upon a dynamic heat transfer model of the instrument. Time-dependent heat transfer can be modeled using lumped-parameter models that can be readily drawn as equivalent electrical circuits.[7] In these equivalent circuits, heat flow is analogous to electrical current flow, temperature is analogous to voltage, heat transfer pathways are shown as resistors, net heat capacities are shown as capacitors, and heat sources are shown as current sources. These lumped-parameter models have been used to describe dynamic heat transfer in complex assemblies such as electric motors[8] and microelectronics packages.[9] While model parameter values for a given model topology can often be calculated directly based on intrinsic system properties (so-called *white-box* modeling), more flexible *grey-box* approaches estimate optimal values of model parameters from empirical calibration data.[10] We have developed a nonlinear lumped-parameter heat transfer model of the calorimeter which allows the heat flow due to the sample to be calculated based on measured temperatures, measured heater input power, and parameter values estimated from calibration data using system identification methods.[11]

A. Nonlinear lumped-parameter thermal model of the calorimeter

A three-state nonlinear model that captures the heat transfer dynamics of the calorimeter well enough to enable calorimetry with power resolution meeting the 100 mW design objective was developed by iteratively testing models of increasing complexity. An equivalent circuit depiction of the model is shown in Fig. 5. To help model the large temperature gradients in the thermally thick insulating firebrick region, this three-state model includes an unmeasured state (T_c) which we associate with a location approximately halfway through the thickness of the insulating firebrick cylinder. The

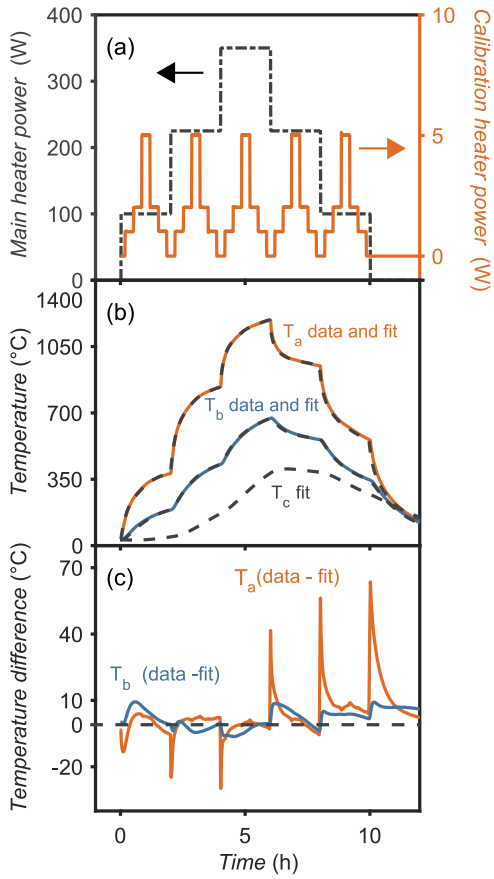

FIG. 6. Calibration experiment input powers, measured system temperature response, model fits, and fit residuals. (a) Time-varying input powers to the main heater and calibration heater, both of which are 0 W at *time* = 0. (b) Temperature response of the instrument to the inputs as measured experimentally and as simulated with the model using the optimized parameter values. Only simulated data are shown for T_c as this is an unmeasured node. The fits of the simulated temperatures to the measured data are shown in dashed lines (c) Temperature residuals (data less fit) for the T_a and T_b nodes. The poor fit at the T_a node near the large step changes in the main heater power indicates that the high-frequency dynamics of the T_a node are not very well described by the present model and that additional model refinement in that region would be beneficial.

model is described mathematically by Eqs. (1a)–(1g). In these equations, Q_{ij} indicates a heat flow from node i to node j and $Q_{i,stored}$ indicates a heat flow into heat capacity i. The temperatures and parameter values are as indicated in Fig. 6. The model conductances and heat capacities are nonlinear up to second-order in temperature (i.e., proportional to T^2); the model can therefore employ up to 30 scalar parameters, although we

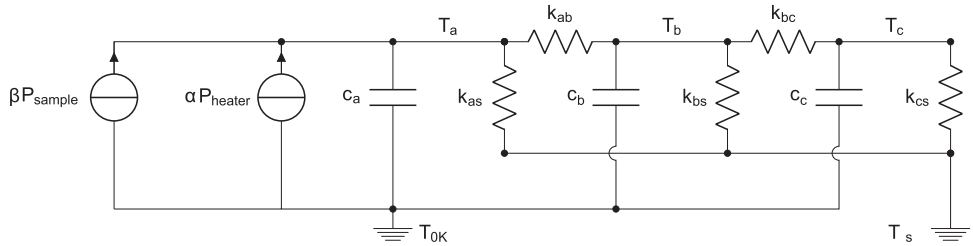

FIG. 5. The two-source, three-state, lumped-element heat flow model of the instrument used to infer the sample power from temperature data. The power from the sample or from a calibration heater at the sample position, P_{sample}, and the power from the main heater P_{heater} are modeled as current sources with temperature-dependent scale factors α and β, which account for the temperature dependence of the radiative and conductive coupling of the heat sources to the sensors. Heat capacities at the nodes i are modeled as capacitors c_i and conductances between nodes i and j are modeled as conductances k_{ij}.

found that not all of those are needed to produce high quality fits to experimental data. The model equations, a set of model parameter values, and power input data can be used to simulate the time-dependent temperature $T_{i,simulated}$ at each model node $i \in \{a, b, c\}$,

$$\frac{dT_a}{dt} = \frac{1}{c_a}\left(\beta P_{sample} + \alpha P_{heater} - k_{as}(T_a - T_s) - K_{ab}(T_a - T_b)\right), \tag{1a}$$

$$\frac{dT_b}{dt} = \frac{1}{c_b}\left(k_{ab}(T_a - T_b) - k_{bs}(T_b - T_s) - k_{bc}(T_b - T_c)\right), \tag{1b}$$

$$\frac{dT_c}{dt} = \frac{1}{c_c}\left(k_{bc}(T_b - T_c) - k_{cs}(T_c - T_s)\right), \tag{1c}$$

where

$$c_i = c_{i,0} + c_{i,1}T_i + c_{i,2}T_i^2, \qquad i \in \{a, b, c\}, \tag{1d}$$

$$k_{ij} = k_{ij,0} + k_{ij,1}T_i + k_{ij,2}T_i^2, \qquad ij \in \{as, ab, bs, bc, cs\}, \tag{1e}$$

$$\alpha = \alpha_0 + \alpha_1 T_a + \alpha_2 T_a^2, \tag{1f}$$

$$\beta = \beta_0 + \beta_1 T_a + \beta_2 T_a^2. \tag{1g}$$

Averaging is used to map the fourteen channels of thermocouple data into the three measured nodal temperatures in the model: T_a is the average of TC1 and TC2, T_b is the average of TC3-TC8, and T_s is the average of TC9-TC15 (isothermal jacket thermocouples). Once the model parameters have been estimated, the thermal power absorbed or generated by the sample can be inferred from temperature data according to the equation

$$P_{sample} = \frac{1}{\beta}\left[\frac{1}{C_a}\frac{d}{dt}T_a + k_{as}(T_a - T_s) + k_{ab}(T_a - T_b) - \alpha P_{heater}\right], \tag{2}$$

where P_{heater} is the measured input power to the heater, $\{T_a, T_s, T_b\}$ are time-dependent temperature data, and $\{c_a, k_{as}, k_{ab}, \alpha, \beta\}$ are model parameters estimated from calibration data.

B. Estimation of model parameters from calibration data

Two calibration experiments were performed to obtain estimates of the three-state model parameters and to track fluctuations in the parameter estimates from run to run. One of these calibrations was performed before and one was performed after the exothermic process simulation experiment described in Sec. V C. Run-to-run fluctuations in the estimated parameter give an indication of the extent of mechanical changes occurring in the instrument due to thermal cycling. In these calibration experiments, high amplitude, wide bandwidth power inputs were applied both to the main furnace heater and to a secondary electrical calibration heater comparable in size to a sample crucible and placed at the sample position. The input power profiles applied to both heaters during these calibration experiments are shown in Fig. 7(a). This calibration routine was designed to perturb the system over a large range of amplitudes and frequencies in order to obtain low uncertainty estimates of the parameters which describe the nonlinear heat transfer dynamics of the instrument. Although the input power

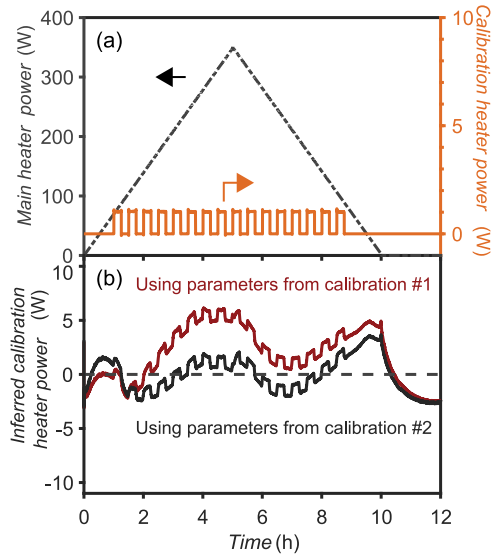

FIG. 7. Summary of calorimetric data from the exotherm simulation experiment. (a) The input powers to the main and calibration heaters. (b) The calibration heater power as inferred using the two different calibrations. The difference between the two inferred power curves suggests that some run-to-run fluctuations are occurring in the instrument. The input power pulses are clearly recovered despite a baseline of several watts. We attributed this baseline to imperfect modeling of the heat flows by the lumped-element model. A model artifact due to the rapid change in the sign of the main heater input power ramp rate is clearly visible in the inferred sample power at 5 h.

profiles used here for calibration were determined heuristically, analytical protocols to minimize uncertainty in parameter estimates are available.[12] The three-state model parameters were then estimated using a two-step optimization procedure.

The first optimization step employed the MATLAB System Identification Toolbox™ function *nlgreyest* (estimate nonlinear grey-box model parameters).[13] The *nlgreyest* function calculates the temperature response $T_{i,simulated}$ at each model node $i \in \{a, b, c\}$ as predicted by Eqs. (1a)–(1g). This temperature response depends on the time, the measured heater input powers, and the model parameter vector θ; *nlgreyest* estimates the optimal value of θ by iteratively varying θ so as to minimize the cost function

$$V(\theta) = \frac{1}{N_{samples}}\left(\sum_{t=1}^{N_{samples}}\left(T_{a,measured}(t) - T_{a,simulated}(t,\theta)\right)^2 + \left(T_{b,measured}(t) - T_{b,simulated}(t,\theta)\right)^2\right), \tag{3}$$

where t is the discretized time running from the first sample time ($t = 1$) to the last sample time ($t = N_{samples}$). This cost function uses data only for the T_a and T_b nodes as T_c is a virtual node with no corresponding data and T_s is an input to the model not a simulated state. During this first optimization step, the β_i parameters of our three-state model were fixed at values of $[\beta_o, \beta_1, \beta_2] = [1, 0, 0]$, while all the other model parameters were optimized using *nlgreyest* (except some unneeded nonlinearities that were turned off). Fixing the β_i parameters allowed the large-scale behavior of the system to be modeled without skewing the β_i parameters towards improving the global model fit at the expense of less accurately modeling the response to heat fluxes from the sample volume. For the two calibration experiments, normalized root mean square error (NRMSE) values near 99% were obtained for the fit between measured

and simulated temperatures. Parameter uncertainties were on the order of 5% (exact estimated parameter values and uncertainties are given in Table SI of the supplementary material). The normalized root mean square error used here is defined in the following equation:

$$NRMSE_i = 1 - \frac{\sum_{t=1}^{N_{samples}} \left(T_{i,measured}(t) - T_{i,simulated}(t)\right)^2}{\sum_{t=1}^{N_{samples}} \left(T_{i,measured}(t) - \bar{T}_i\right)^2}. \quad (4)$$

In the second step of the optimization, we optimized the parameters $[\beta_o, \beta_1, \beta_2]$ to enable accurate recovery of the sample power. This optimization process proceeded as follows: the inferred calibration heater power obtained using $[\beta_o, \beta_1, \beta_2] = [1, 0, 0]$ was plotted, and the energies corresponding to the most well-defined portions of the plot were obtained by integration of the inferred power (Fig. S4 of the supplementary material); these peak energies were then normalized by the true energies known from the input power profile; the normalized energies were then plotted against the peak midpoint temperatures and a second-order polynomial was fit to this plot (Fig. S5 of the supplementary material); the three resulting fit coefficients were used directly as the beta parameters. This process was performed for both calibration experiments, yielding two sets of $[\beta_o, \beta_1, \beta_2]$ parameters, also given in Table SI. Uncertainties were not computed for the beta parameters obtained in this way.

C. Calorimetry of a simulated exothermic process

Using the calibration heater, we conducted an experiment simulating exothermic processes at the sample location at several different temperatures. In this experiment, the main heater input power was ramped linearly from 0 W to 350 W and back to 0 W symmetrically over the course of 10 h. This input power ramp caused T_a to undergo approximately linear temperature ramps between room temperature and 1114 °C. During this time, an exothermic process at the sample location was simulated by switching the input power to the calibration heater between 0 W and 1 W for 15-min periods (corresponding to 900 J exotherms). The power inputs are plotted in Fig. 7(a). The inferred calibration heater power during the experiment is plotted in Fig. 7(b), wherein the data are inferred using the model parameters estimated both from the calibration experiment before (calibration #1) or after (calibration #2) the exotherm simulation experiment. The raw data for the inferred power feature a broadband noise of ~5 W amplitude on top of a slow-moving calorimetric signal (Fig. S3 of the supplementary material). This raw inferred power is processed with a moving-average filter with a 80 s span to produce the data plotted in Fig. 7(b).

The inferred power plotted in Fig. 7(b) shows that the 900 J/1 W heater pulses can be recovered with approximately the correct amplitude, despite a slowly changing baseline of several watts. We attribute this baseline to heat transfer processes that are not fully captured by our lumped-element model and which cause a small fraction of the main heater power to be included in the inferred calibration heater power. This attribution is supported by an experiment we performed where the calibration heater was not turned on (Fig. S6 of the supplementary material), in which the residual between the measured and inferred main heater powers is of similar magnitude and bandwidth to the baseline of the inferred calibration heater power shown in Fig. 7.

One possibility for improving the model is to add an additional temperature node with a long time constant; this could help more accurately model slow heat storage processes which might be contributing to the observed baseline. Other modifications to the model topology that more completely utilize the available thermocouple data might also decrease the observed baseline. The marked difference in baseline between the two calibration data sets further suggests that physical changes in the instrument between experiments may directly affect heat flows and thus the model parameters. However, this assertion is complicated by the fact that the run-to-run change in the estimated model parameters is comparable to the magnitude of the uncertainty of the estimated parameters. At best, one may infer that a combination of model deficiencies and physical changes in the instrument contribute to imperfect data reproducibility.

Baseline subtraction can enable the integration of a calorimetric peak on top of a large instrumental baseline with some degree of accuracy if the peak is sufficiently distinct from the baseline. In the present case, the rectangular heat pulses are quite clear and the peak areas can be integrated using a semi-manual approach employing a MATLAB script where a user chooses the beginning and end points for integration with a cursor, a linear baseline connecting the endpoints is subtracted, and the remaining area under the peak is calculated. Energies calculated by integration of the areas under the input-power pulses are plotted in Fig. 8.

Different energies are inferred utilizing parameters from the calibration experiment before (895 ± 56 J, 99.46% ± 6.32% of 900 J, 1σ uncertainty) or after (886 ± 55 J, 98.50% ± 6.10% of 900 J, 1σ uncertainty) the sample-simulation experiment. From these results, we estimate the energy measurement accuracy of the calorimeter utilizing the model and measurement protocol presented here to be ≤6.35% over the 150–1100 °C temperature range of the experiment. We calculate this accuracy by taking the square root of the sum of the squares of the

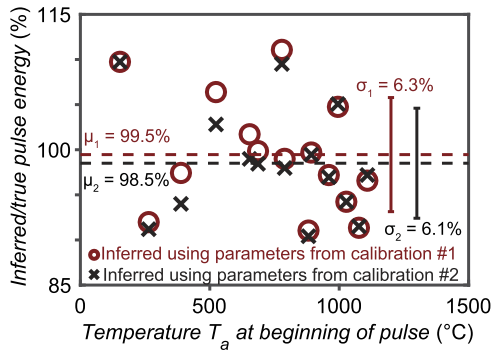

FIG. 8. Normalized inferred pulse energies from the sample-simulation experiment, using parameters from calibration prior to (red circles, μ_1, σ_1) and after (black ×'s, μ_2, σ_2) that experiment. The heater-delivered pulses of 1 W for 15-min intervals (900 J/pulse). The vertical bars are centered at the mean of each data set and span ±1 standard deviations (±1σ).

systematic error (deviation of the mean energy from 100% of 900 J) and the random error (standard deviation of the data points) from the inferred energy data points. The power resolution of the measurement scheme is approximately 50 mW, although this depends heavily on the low-pass filter employed to remove high-frequency noise in the data, as illustrated in Fig. S3 of the supplementary material.

VI. EXTENSIONS TO THE MEASUREMENT CAPABILITIES

Here we identify possible future improvements to our apparatus and refinements to the data analysis procedures that may be of utility to interested workers. In particular, the calorimetric accuracy can be improved and increased operating pressures and temperatures should be possible.

1. Improving the mechanical stability of the instrument, especially the poorly constrained tip positions of the most important thermocouples, TC1 and TC2, to minimize run-to-run physical variations should improve the reproducibility of the calibration and therefore the accuracy of the measurement.
2. The calorimetric accuracy could be improved by a modified furnace configuration wherein the heater power is used to heat an isothermal boundary which surrounds the sample and temperature sensors. This proposed approach is similar to contemporary differential scanning calorimeters except that the differential measurement is taken through subsequent apparatus runs. In such a configuration, the furnace wall between the heater and the sample tube becomes the thermal ground in the lumped-element model, and fewer model parameters would be required because the heater power input and the model elements associated with the thermal mass and thermal conductances of the furnace vanish from the model. The simpler resulting model would deal only with the dynamics of the heat flows from the sample through the sensor(s) to the furnace wall and the slow heat flows through the furnace insulation need not be modeled at all.
3. The systematic portion of the inferred power baseline [Fig. 7(b)] suggests there is an unmodeled apparatus behavior, most likely an additional state (capacitor and resistor), corresponding to slow propagation of heat through the thermally thick furnace insulation. The present apparatus already needs a large parameter set, so adding more states was not practical in this work; however, the simpler model enabled by the modified instrument noted in (2) is a good candidate for this approach to baseline reduction.
4. Improved estimates of the model parameters might also be obtained by using optimized calibration routines rather than heuristically chosen ones.[12]
5. High-temperature operation at pressures well beyond 33 bars should be possible with a reaction tube of low-porosity alumina or another suitable material. Our simple pressure vessel calculations predict a rupture pressure of 221 bars for the alumina reaction tube employed, although a more accurate prediction of rupture pressure would consider stresses induced by temperature gradients and defects in the alumina.[14]
6. The maximum operating temperature of the presented design is limited by the melting point of the resistive heater, which can be readily replaced with a silicon carbide heater suitable for operation up to 1650 °C.
7. At lower operating pressures, we have had preliminary success using a quartz reaction tube that provides optical access to the sample under investigation.
8. Higher-pressure and lower-temperature operation should also be feasible with metal reaction tubes (e.g., steel and Hastelloy) as demonstrated by Mauron *et al.*[6]

VII. CONCLUSIONS

We have presented an instrument for measuring heat flows and pressure changes resulting from high-temperature reactions between gram-scale samples and high-pressure reactive gases. Operation of the instrument at 1232 °C under 33 bars of pure H_2, with a low leak-rate of 2.28 ml bars h^{-1} and pressure measurement resolution of 0.005 bars, has been demonstrated. A nonlinear, lumped-parameter heat transfer model of the instrument, with parameter values estimated using grey-box system identification techniques and calibration data, was used to infer heat flows at the sample position from experimental temperature data. A validation experiment using an electrical calibration heater at the sample position to deliver 900 J pulses (1 W over 15 min) was used to demonstrate a calorimetric power resolution of 50 mW and an energy measurement accuracy of 6.35% over the temperature range 150–1100 °C.

The calorimetric scheme presented here has two key advantages. First, the temperature sensors and furnace heater elements are separated from the reactive gas space, enabling experiments with reactive gases to be carried out routinely without chemical degradation of the furnace or temperature sensors. Second, the use of a lumped-element thermal model of the calorimeter calibrated with system identification techniques grants much more freedom in the geometric configuration of the sample, heater, and sensors than do calorimetry schemes that employ a single calibration factor. While the instrument geometry and model must both be clearly optimized to achieve high accuracy, this concept of model-based calorimetry using system identification can enable calorimetric measurements to be performed when practical constraints preclude the application of more conventional calorimetric techniques.

The instrument presented here will provide information on the thermodynamics and kinetics of a range of candidate heterogeneous chemical reactions for emerging applications such as thermochemical energy storage schemes utilizing metal hydrides.

SUPPLEMENTARY MATERIAL

See supplementary material for additional tables and figures (Appendix A), an expanded discussion of the design objectives (Appendix B), and a brief note on ceramic pressure vessel design (Appendix C).

ACKNOWLEDGMENTS

We thank UBC Chemistry Mechanical Engineering Services and the Chemical and Biological Engineering Workshop for their assistance with instrument fabrication. We acknowledge Google Inc. for financial support. Mikhail Dikovsky and Matt Trevithick made important contributions to this collaboration. This research was supported in part from the Canada First Research Excellence Fund, Quantum Materials and Future Technologies Program, Natural Sciences and Engineering Research Council of Canada, Canada Foundation for Innovation, Canadian Institute for Advanced Research, Canada Research Chairs, and the Stewart Blusson Quantum Matter Institute (QMI). BPM acknowledges QMI's Quantum Electronic Science and Technology Initiative.

[1]P. Pardo, A. Deydier, Z. Anxionnaz-Minvielle, S. Rougé, M. Cabassud, and P. Cognet, Renewable Sustainable Energy Rev. **32**, 591 (2014).
[2]L. André, S. Abanades, and G. Flamant, Renewable Sustainable Energy Rev. **64**, 703 (2016).
[3]D. A. Sheppard, M. Paskevicius, T. D. Humphries, M. Felderhoff, G. Capurso, J. Bellosta von Colbe, M. Dornheim, T. Klassen, P. A. Ward, J. A. Teprovich, C. Corgnale, R. Zidan, D. M. Grant, and C. E. Buckley, Appl. Phys. A **122**, 395 (2016).
[4]G. Sandrock, J. Alloys Compd. **293**, 877 (1999).
[5]K. Chłopek, C. Frommen, A. Léon, O. Zabara, and M. Fichtner, J. Mater. Chem. **17**, 3496 (2007).
[6]P. Mauron, M. Bielmann, V. Bissig, A. Remhof, and A. Züttel, Rev. Sci. Instrum. **80**, 95113 (2009).
[7]G. Sidebotham, *Heat Transfer Modeling: An Inductive Approach* (Springer International Publishing, Cham, Switzerland, 2015).
[8]O. I. Okoro, IEEE Trans. Energy Convers. **20**, 730 (2005).
[9]F. Christiaens, B. Vandevelde, E. Beyne, R. Mertens, and J. Berghmans, IEEE Trans. Compon., Packag., Manuf. Technol., Part A **21**, 565 (1998).
[10]T. P. Bohlin, *Practical Grey-Box Process Identification: Theory and Applications* (Springer-Verlag, London, England, 2006).
[11]L. Ljung, *System Identification: Theory for the User*, 2nd ed. (Prentice Hall, Upper Saddle River, NJ, 1999).
[12]G. C. Goodwin, Proc. Inst. Electr. Eng. **118**, 922 (1971).
[13]L. Ljung, System Identification Toolbox^{TM} Reference, The Mathworks, Natick, MA, 2016.
[14]H. Abe, M. Naito, T. Hotta, N. Shinohara, and K. Uematsu, J. Am. Ceram. Soc. **86**, 1019 (2003).